

# High-frequency electromagnetic induction sensing of non-metallic materials

John B. Sigman, Benjamin B. Barrowes, Kevin O'Neill, Yinlin Wang, Janet E. Simms, Hollis H. Bennett Jr., Donald E. Yule, and Fridon Shubitidze

**Abstract**—We introduce a frequency-domain (FD) Electro-magnetic Induction (EMI) instrument for detection and classification of objects with either high ( $\sigma > 10^5 \text{ S/m}$ ) or intermediate ( $1 < \sigma < 10^5 \text{ S/m}$ ) electrical conductivity. While high-conducting metallic targets exhibit a quadrature peak response for frequencies in a traditional electromagnetic induction regime under 100 kHz, the response of intermediate-conducting objects manifests at higher frequencies, between 100 kHz and 15 MHz. Materials such as carbon fiber or conducting salt solutions exhibit conductivities in this intermediate range and are undetectable by traditional low-frequency EMI instruments. To detect these intermediate-conducting targets, we developed a high-frequency EMI (HFEMI) instrument with a frequency range extended to 15 MHz. The HFEMI instrument requires novel hardware considerations, coil design, and data processing schemes. Most importantly, the wire length of transmit and receive coils are shorter than traditional-frequency EMI sensors, so that the phase on the transmit and receive coils is near constant. We present hardware and software aspects of the HFEMI instrument along with preliminary data, demonstrating its ability to detect intermediate-conducting objects.

**Index Terms**—Electromagnetic Induction, Coils, Remote sensing, Conductivity, Frequency domain analysis.

## I. INTRODUCTION

INTERMEDIATE electrical conductivity (IEC) materials ( $1 < \sigma < 10^5 \text{ S/m}$ ), such as carbon fiber (CF), have been used in many civilian and military applications. For example, because of recent advances in munition technologies, the US military now uses smart bombs, which are made with CF. These new CF munitions are used for precision strikes and minimize collateral damage by reducing shrapnel from the bomb [1].

In addition, CF and other IEC materials have been actively used in home-made explosives (HME) [2]. Accordingly, detection and remediation of CF unexploded ordnance (UXO) and HME have become a high priority for the military. Unlike metal shells, which explode and scatter shrapnel, the carbon fiber shell is vaporized on detonation. Although this gives smart bombs a more intense local blast radius, and means cleanup efforts should be focused on detection of intact bombs, there is still a pressing need to classify between CF UXO and man-made CF clutter. This task is not simple because of the physical properties of CF.

IEC materials are less conductive than metallic targets, and as a result they are undetectable by present-generation advanced electromagnetic induction (EMI) instruments. To

address this need, we have developed an EMI sensor that can detect and classify subsurface discrete IEC targets by extending the range of frequencies used for traditional EMI. In the next section, we will explain some of the pertinent physics, and why higher frequencies are required for detection of CF discrete targets by EMI. Later in this paper, we will detail how these higher frequencies require shorter coils to preserve magnetic field spatial distribution and azimuthal symmetry.

## A. Background

According to Lenz's law, a conducting object in a primary alternating magnetic field will develop eddy currents to oppose the changing flux inside the object [5]. In turn, these eddy currents produce a secondary alternating magnetic field, which is out of phase with the primary field. We call the component of the eddy current synchronized with the primary field "in phase", and the component  $90^\circ$  out-of-phase with the primary field "quadrature". Three salient features – a linear range, a quadrature peak, and an inductive limit – of the secondary field are shown in Figure 1. The three ranges occur at different frequency ranges for different objects, but always in the same order [6], [7].

At low frequencies, the eddy currents flow through the bulk of the object [8]. They are  $90^\circ$  out-of-phase with the primary

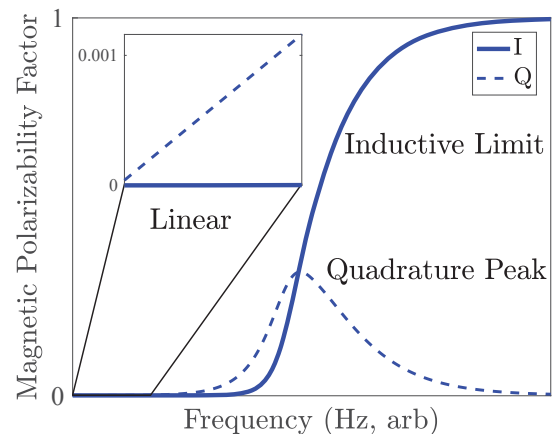


Fig. 1. In-phase and quadrature components of an EMI relaxation response for a conducting, non-permeable sphere [3]. The applicable frequency range and magnitudes are governed by geometry, permeability, and conductivity [4]. Scales on the axes depend on object properties and the measurement configuration. The window in the upper-left corner is to show the proportionality of the quadrature component to frequency for the lower range, as the scale would otherwise make this difficult to observe.

magnetic field, and have magnitude that grows proportionally to the frequency of the magnetic field. The upper-left corner of Figure 1 includes a window of the lowest frequencies, showing a negligible in-phase portion and proportional quadrature component. In the linear range, material resistivity limits the magnitude of the secondary field. This range is not normally used to characterize UXO targets, but is used for applications such as resistivity estimation of soil [9].

The full wavenumber for electric and magnetic fields is given by  $k^2 = \mu\epsilon\omega^2 - j\mu\sigma\omega$ , where  $\sigma$  is the material electrical conductivity,  $\mu$  is the magnetic permeability,  $\epsilon$  represents permittivity, and  $\omega$  is the angular frequency. Because the ratio between the two terms of the wavenumber is  $\frac{\sigma}{\omega\epsilon}$ , for conducting materials with everyday permittivity (on the order of water or less), we observe that the diffusive term dominates, and we can neglect displacement currents [10]–[12] (for a more in-depth discussion of this phenomenon, see O'Neill [13]). The wavenumber  $k$  can be expressed in the diffusive limit as  $k = \sqrt{-j\sigma\omega\mu}$ . If written  $k = \gamma + j\gamma$ , then the real part of the wavenumber expresses traveling oscillations inside the object, and the imaginary part describes the exponential decay over space, i.e., skin depth effects. The frequencies that correspond to half “wavelengths” (from the real portion of  $k$ ) fitting neatly inside one dimension of an object [14] create an EMI diffusion resonance. The resonance causes a peak response in the quadrature component of the secondary field and an inflection point of the in-phase component. The frequency of the quadrature peak is a result of object properties such as size, conductivity, permeability, and shape. In turn, these properties are linked to object and signal features central to inversion and classification. IEC materials the size of most UXO exhibit this peak in the HFEMI band of 100 kHz–15 MHz [2], [15], see Figure 2.

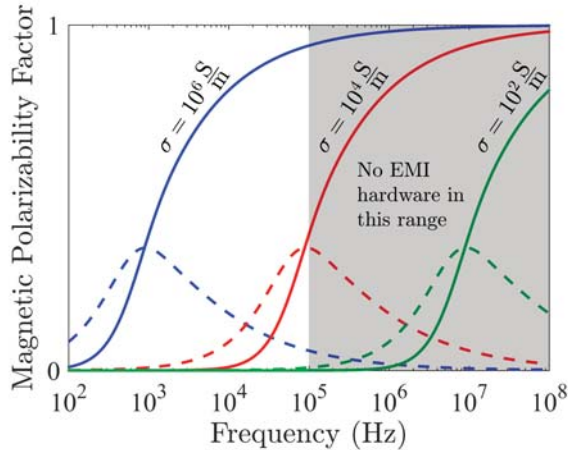


Fig. 2. EMI response for three 8 cm spheres of different electrical conductivities [3]. The real parts of the magnetic polarizability factor have solid lines, and the imaginary parts have dashed lines. Present-generation EMI sensors do not use frequencies above 100 kHz, making intermediate- and low-conductivity objects undetectable. Larger targets have quadrature peaks at lower frequencies, as do higher conductivity targets.

As the frequency of the primary field increases further, the eddy currents move to the surface of the object, and the secondary  $\vec{B}$  field plateaus in the inductive limit.

## B. Existing Methods

Ground penetrating radar (GPR) could be applied to the detection of objects producing dielectric or conductivity contrasts [16], [17], and could potentially be used for the detection of IEC objects. However, at GPR frequencies ( $> 50$  MHz), the incident field typically reflects from plentiful nearby dielectric heterogeneities and clutter, producing substantial signal clutter and placing conventional GPR at a disadvantage relative to EMI sensing [17].

Two general classes of EMI instruments are used today for geophysical detection and discrimination [13]. Time-domain (TD) EMI instruments pulse electrical current in a transmit loop, and register secondary field responses in the absence of a primary field. These instruments are the most popular for metallic targets classification, and because there is no need to separate primary and secondary fields, arrays of receivers can observe rich spatial information [18], [19]. The diversity of EMI data from targets using such an array facilitates inversion [8], [20], [21].

Established TD instruments also show distinctive patterns in responses from metallic objects, and these are linked to the same physical effects that produce the notable frequency-domain (FD) activity. This correspondence between the time and frequency domains means that the observable band is limited by time-domain parameters. Established TD instruments cannot be used for HFEMI because of practical hardware limitations. If the observable band of a target’s relaxation is limited by  $f_{max} = \frac{1}{\Delta t}$  (where  $\Delta t$  is the transience of the primary field turnoff), then 15 MHz bandwidth requires  $\Delta t = 67ns$ , which is currently not feasible [22].

The other broad class of EMI sensors consists of frequency-domain instruments, which have also been successful in detecting and classifying buried targets [23], [24]. Here, the target is illuminated by a primary field, which is produced by a continuous waveform instead of a pulse. Because the transmitter is on during data acquisition, the primary field will overwhelm signal at the receiver. Therefore, either high dynamic range or geometric nulling is required to acquire data with a sufficiently high SNR for classification.

The HFEMI band is not completely new to subsurface sensing and has been used for EMI via the Very Early Time Electromagnetic (VETEM) instrument [25] and for GPR [26]. In the case of the VETEM instrument, induction data were combined with spatial data to create maps of conductive soils. When the range was used for GPR, frequencies as low as 12.5 MHz were used to achieve deep ground penetration. The Laboratory for Advanced Subsurface Imaging (LASI) high-frequency ellipticity system also used low-frequency GPR, 31–32 MHz [27], for subsurface waste sensing. Our new HFEMI instrument is the first to use these frequencies on discrete targets to extract electromagnetic relaxation signatures.

In this paper, we will first discuss hardware and coil design. Next, we will present our magneto-quasistatic model and calibration techniques for extracting target polarizability curves from measured data. Lastly, we will show preliminary data, suggesting agreement with models for several different targets.

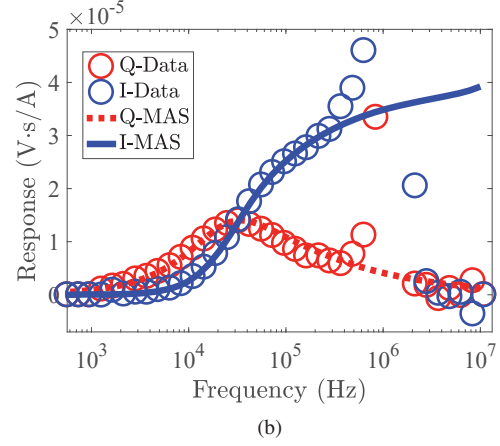
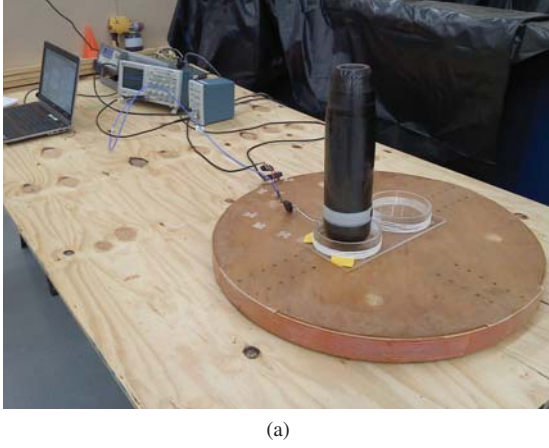


Fig. 3. (a) An early prototype HFEMI instrument with the 14-turn, 1-m diameter MPV transmitter coil and a homemade figure-8 receiver coil. The target here is a 105-mm UXO made of carbon fiber. (b) Data and model for this setup. Modeling of the target's polarizability was done by the Method of Auxiliary Sources (MAS) [15], [29], [30].

## II. HFEMI PHYSICS

### A. Introductory Experiments

The work described here extends the frequency range for EMI instruments. A logical starting point for this research is to only replace control hardware and use existing EMI coils. For our first experiments, we built a prototype using a single man-portable vector (MPV) sensor transmitter [28] and a hand-wound receiver. The MPV sensor is an advanced time-domain induction sensor, and its transmitter has 14 wire turns with 1-m diameter. The receiver was a 10 cm figure-8 design with 10 wire turns. We connected this transmitter (Tx)/receiver (Rx) pair to an oscilloscope, function generator, and current probe; and used it to measure carbon fiber targets in the higher frequency band of 100 kHz–15 MHz. We show a photograph of this experimental setup in Figure 3a. As shown in Figure 3b, data and modeled response agree at low frequencies, but not in the HFEMI band above about 500 kHz. These data were processed by a scheme we will detail later in Section IV of the paper, and reflect “object minus background, not the complete “object minus background divided by ferrite minus background” treatment, and thus have different  $y$ -axis units from the results shown later in this paper. In this case, the more advanced signal processing treatment would not have made a meaningful difference.

Figure 4 shows full 3D EM modeling of the magnetic field from the transmitter. The field, shown in Figure 4e, exhibits poles at the same high frequencies where model and data disagree. To explain this effect, we will first consider how the high frequencies of HFEMI sensing affect the magnetic coupling between coils and targets.

### B. Magnetic Coupling

Consider a transmitter, receiver, and conducting target. For now, we assume either perfect background subtraction or perfect geometric nulling, and the responding target's position and orientation relative to the Tx/Rx pair is unknown. For simple targets, such as thin loops, the full 3D system of the

target's geometry, orientation, and material can be represented by the product of a coupling term and response function [6], [32],

$$V_R(\omega) = M_{OR}\beta_O(\omega)M_{TO}i_T(\omega) \quad (1)$$

where  $V_R$  is the voltage measured in the receiver,  $i_T$  is the measured transmitter current, and  $\beta_O$  is the object's response function; all are phasors.  $M_{TO}$  and  $M_{OR}$  represent the inductive coupling from the transmitter to the object and object to the receiver, respectively. This model does not hold exactly for more complicated targets, but is nonetheless a useful approximation [33]. Because  $V_R$  and  $i_T$  are measured, there is only one unknown with frequency dependence in Equation 1,  $\beta_O$ . This means that after sweeping frequencies, we can extract the response function with the only ambiguity a proportionality of  $(M_{TO}M_{OR})^{-1}$ , which depends primarily on the measurement configuration.

This model only holds for existing instruments in a typical induction frequency regime (30 Hz – 100 kHz). A special instrument is required for this model to suit HFEMI sensing. In this section, we will show two ways that the coupling terms can include frequency dependence, where they didn't at normal induction frequencies.

*a) Transmitter-Object Coupling:* The inductive coupling of the transmitter and object,  $M_{TO}$ , is the ratio of induced electromotive force (emf) in the target to change in the transmitter current. This emf is induced by the alternating primary field, which is produced by electrical currents in the transmitter. At any frequency, the dyadic Green's function for magnetic field at an object's location, due to a current density  $\vec{J}$  in the Tx, is given by [34]

$$\mathbf{G}_{TO} = \frac{1}{4\pi} e^{jkR_{TO}} \left( \frac{1}{R_{TO}^3} - \frac{jk}{R_{TO}^2} \right) \begin{bmatrix} 0 & R_z & -R_y \\ -R_z & 0 & R_x \\ R_y & -R_x & 0 \end{bmatrix} e^{-j\omega t} \quad (2)$$



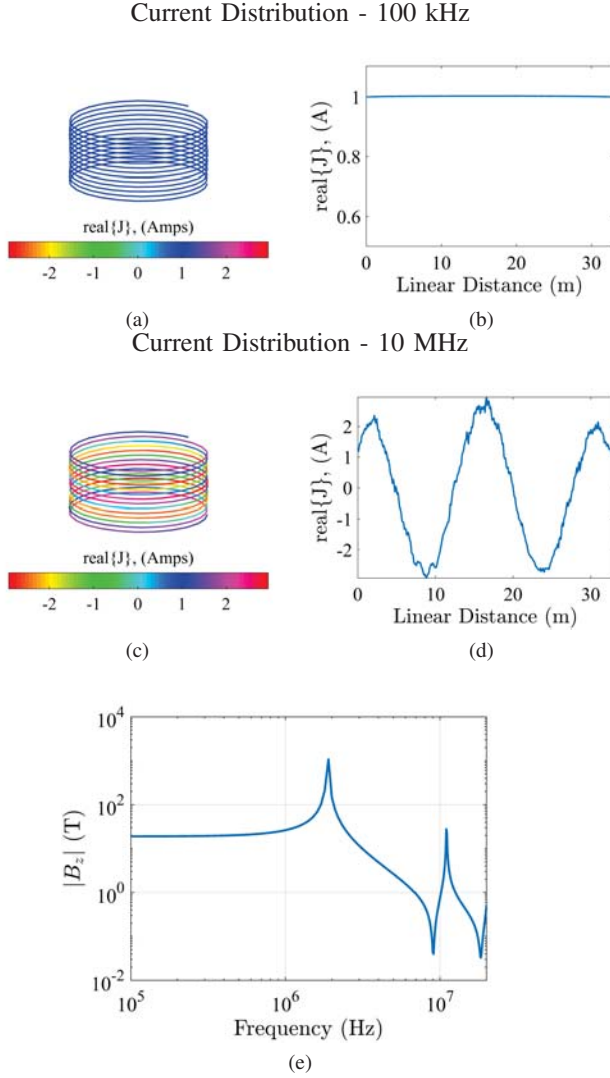


Fig. 4. EM modeling (using EMCOS [31]) of current distribution on the large MPV coil transmitter at (a) low and (c) high frequency. The real portion of the frequency-domain current along the path of the loop is plotted at (b) low frequency and (d) high frequency. In these simulations, the imaginary portion of the same current is effectively zero. The  $z$  axes of plots (a) and (c) have been stretched for easier viewing. (e)  $B_z$  vs. frequency in the center of the transmitter.

where  $\vec{R}_{TO} = \vec{r}_O - \vec{r}_T$  is the vector from the transmitter to the object,  $R_{TO} = |\vec{R}_{TO}|$ , and  $k$  is the wavenumber for the surrounding media. In the frequency domain in linear media, every field value varies as  $e^{-j\omega t}$ , and this term is suppressed everywhere after Equation 2. Assuming a line current Tx, the  $\vec{H}^{pr}$  field produced by the transmitter path  $C$  is

$$\vec{H}^{pr} = \int_C \mathbf{G}_{TO} \cdot \vec{J}(\ell, \omega) d\ell \quad (3)$$

When the magnitude of the current,  $I = |J|$ , is uniform along the wire, then the Tx current only contributes a fixed, or known geometrical factor in the evaluation of the integral.

$$\vec{H}^{pr} = I(\omega) \int_C \mathbf{G}_{TO} \cdot \hat{j}(\ell) d\ell \quad (4)$$

where  $\hat{j}(\ell)$  is a unit vector ( $\hat{j}(\ell) = \vec{J}(\ell)/|\vec{J}(\ell)|$ ) along the Tx current path  $C$ .

Crucially, there are two places in the expression for a primary field that involve frequency dependence. The first, exhibited by every appearance of  $k$  in Equation 2, involves diffusive effects or propagation *in the medium* and is shown pictorially in Figure 5 by  $\vec{R}_{TO}$ . In free space, the range of EMI sensing is kept so short that propagation and retarded time can be neglected. Even at HFEMI frequencies, the shortest wavelength in free space is 20 m, considerably larger than typical separation between instrument and target. Such (potential) wave effects enter through the first, real-valued term in the expression for  $k$ . In conducting media, such as sea water, the second (conductive, imaginary) term in  $k$  may come into play significantly. In particular, diffusive effects can change electromagnetic coupling between transmitter and object. This can usually be ignored at traditional induction frequencies, but will be important at HFEMI frequencies in a conductive environment. Nevertheless, this type of change in the magnetic coupling can be readily calculated, given knowledge of the environment, and should not inhibit the extraction of the response of a discrete target.

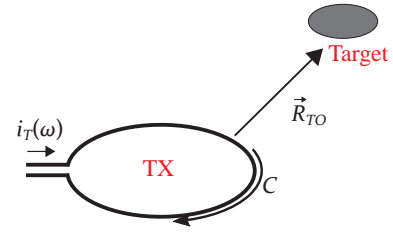


Fig. 5. Coupling between the target and the transmitter. The mutual inductance between transmitter and object,  $M_{TO}$ , is frequency dependent for larger separation between the two,  $\vec{R}_{TO}$ , or longer arc length around the coil,  $C$ .

The other way that frequency affects magnetic coupling is not through the dimension between the transmitter and the target but in the curled-up dimension of the transmitter coil itself. This is the path integral  $C$  of Equation 3 and is depicted in Figure 5. In Equation 3, the current density along the transmitter coil is written as a function of position and frequency,  $\vec{J}(\ell, \omega)$ . Overall, there can be no uniform current density on a conductor with non-negligible electrical length. E-field propagates in the transmitter wire at the same speed as in the surrounding medium. At higher frequencies, corresponding to shorter wavelengths,  $\nabla \cdot \vec{J} \neq 0$  along the wire. Due to the high conductivity inside the wire, the total current  $J$  represents conduction currents.

In cases with significant variation of the current along the Tx loops, one cannot compute fields and object responses as simply as in past applications, which used a single measured current value for  $I$  in Equation 4. Changes in current may be comparatively gradual along the length of the Tx wire. However, for multi-turn coils with closely spaced windings, strongly contrasting currents appear in close proximity to one another, causing a troublesome heterogeneity in the primary field. In this case, the primary field is no longer axially symmetric with respect to the Tx coil, and is also not an easily predicted function of the input current [35], [36].

Thus, the reason that the result in Figure 3b appears distorted is the contrasting current phase on the curled-up dimension of the Tx loop. The wire length of the large 14-turn MPV coil is longer than free-space wavelengths in the HFEMI range. Consistent HFEMI sensing requires much smaller coils to avoid these effects, reflected by our final Tx and Rx coil designs, discussed in Section III-B.

*b) Object Response:* Continuing with the causal chain of EMI sensing, the primary field induces eddy currents inside the object, which in turn produce a secondary field. At a distance from the target, this secondary magnetic response can be approximated by that from a magnetic dipole. The dipole moment of the responding target,  $\vec{M}$ , is related to the primary field,  $\vec{H}^{pr}$ , and the target's polarizability tensor,  $\mathbf{P}$ , by

$$\vec{M} = \mathbf{P} \cdot \vec{H}^{pr} \quad (5)$$

The eigenvalues of the polarizability tensor are the polarizabilities along the principal axes of the target [37]. For the sake of simplicity, we will consider the target to be a first-order loop, oriented in the  $+\hat{z}$  direction. It's polarizability would then be

$$\mathbf{P} = \beta_O(\omega) \begin{bmatrix} 0 & 0 & 0 \\ 0 & 0 & 0 \\ 0 & 0 & 1 \end{bmatrix} \quad (6)$$

where  $\beta_O(\omega)$  is the scalar, frequency-dependent response function for the loop. It is related to the current induced in the loop for a given frequency [6], [33].

The dyadic Green's function for a magnetic dipole and the resulting secondary field are, respectively [34]

$$\mathbf{G}_{OR} = \frac{e^{jkR_{OR}}}{4\pi\mu} \left( \frac{jk\mathbf{I}}{R_{OR}^2} - \frac{3jk\vec{R}_{OR}\vec{R}_{OR}^T}{R_{OR}^4} + \frac{-\mathbf{I} - k^2\vec{R}_{OR}\vec{R}_{OR}^T}{R_{OR}^3} + \frac{3\vec{R}_{OR}\vec{R}_{OR}^T}{R_{OR}^5} \right) \quad (7)$$

$$\vec{H}^s = \mathbf{G}_{OR} \cdot \vec{M} \quad (8)$$

Combining equations 3, 6, and 8 gives

$$\vec{H}^s = \mathbf{G}_{OR}(\omega) \cdot \left( \left( \beta_O(\omega) \left( \int_C \mathbf{G}_{TO}(\omega) \vec{J}(\ell, \omega) d\ell \right) \cdot \hat{z} \right) \hat{z} \right) \quad (9)$$

*c) Object-Receiver Coupling:* The measured voltage at the receiver is typically written

$$V_R = j\omega N \iint_A \mu \vec{H}^s \cdot d\vec{S} \quad (10)$$

where  $V_R$  is the open-circuited receiver voltage,  $N$  is the number of turns in the transmitter, and  $d\vec{S}$  is the vector normal to the surface of integration,  $A$ . While it is intuitive to think about the flux "cutting" the surface of the receiver and amplified by multiple turns, in the HFEMI range this is an oversimplification of the physics and neglects wave effects at high frequency.

Similar to how we accommodate long receiver paths, Equation 10 must be cast as a line integral

$$V_R = j\omega \oint \vec{A}^s \cdot d\vec{\ell} \quad (11)$$

where  $\vec{A}^s$ , the secondary vector potential, incorporates the magnetic effects from induced currents that would not be allowed on an electrically short, open-circuited receiver loop. At HFEMI frequencies and long coil dimensions, the induced currents will re-radiate some of the energy in the secondary field. Thus, by reciprocity with the transmitter, we must impose the same restrictions on the length of the receiver coil.

For Tx and Rx coils sufficiently short relative to field variations, we can regard the integrand in Equation 11 as constant and cast  $V_R$  conveniently in terms of point values of the relevant quantities [33]

$$V_R(\omega) = M_{OR}(\omega) \beta_O(\omega) M_{TO}(\omega) i_T(\omega) \quad (12)$$

where  $V_R$  is proportional to the flux through the receiver coil, and  $\beta_O$  is the response function, a lumped, scalar version of the polarizability tensor (which we will refer to as the polarizability from here on; see Figure 7 below for clarification of these and related quantities). For the purposes of our procedure, it is important to ensure that the transmitter current is a uniform magnitude and phase along the Tx coil. This guarantees that the primary field for a given point in space is proportional only to the measured current at the input to the transmitter, and not affected by the frequency of the alternating current. Once we understood the discrepancy between measured and modeled data in the HFEMI band – and how it was related to the size of the transmitter coil and its nonuniform current distribution – we reduced the length of the Tx and Rx coils and constructed a new prototype HFEMI instrument.

### III. HARDWARE

#### A. Electronics

For control of the HFEMI instrument, we used the National Instruments VirtualBench all-in-one function generator/oscilloscope. After a data acquisition is initiated, the range of 400 Hz to 15 MHz is swept using logarithmically-spaced frequencies. At each frequency, the Virtual Bench drives a current in the transmit loop. Time-domain samples are logged and integrated into frequency-domain ratios between receive voltage and transmit current. This integration, or stacking, improves SNR by  $10 \log_{10} N$  [25], where  $N$  is the number of logged waveforms at a given frequency. It takes about 1000 waveforms per acquisition to achieve good SNR at low frequencies.

#### B. Transmitter and Receiver

At 15 MHz,  $\lambda = 20$  m in air, and so we chose a 1-turn 25-cm diameter loop for the transmitter. The circumference of the loop is a negligible fraction of the shortest wavelength in our band.

The receiver is a figure-8 loop, with its wire crossing located in the center of the transmitter loop and the loops forming 7.5-cm diameter circles. The windings of the two poles are in opposition, so that a symmetrical flux, i.e., the primary field inside the dipole transmitter or response from a uniform soil background, induces emfs that cancel one another. This geometric nulling reduces the required dynamic range of the

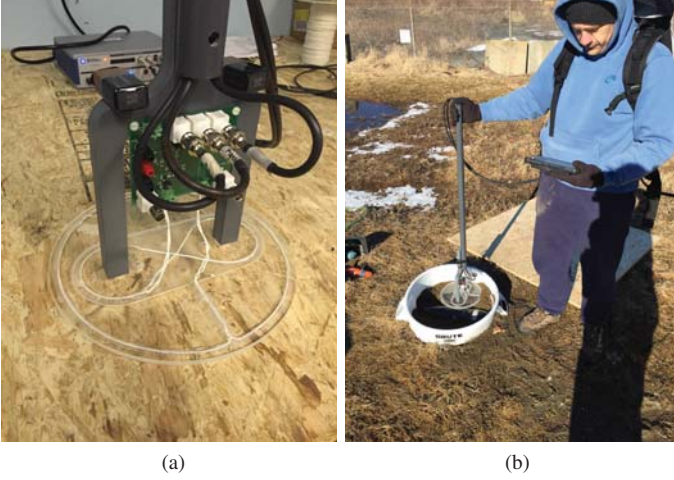


Fig. 6. (a) Prototype HFEMI instrument and (b) its use in the first formal test of the instrument at the Cold Regions Research and Engineering Laboratory (CRREL) in Hanover, NH.

instrument's electronics. The figure-8 design is something of a gradiometer, however, we are not using it to sense a gradient, but instead asymmetries and local perturbations of the secondary field that arise from discrete conducting targets such as UXO.

The open-circuited receiver loop is fed into a buffer amplifier, which has two purposes. Firstly, it boosts the received signal. Secondly, because there is a coaxial cable connecting the receiver to the VirtualBench, this electrically isolates the capacitance of the cable from the inductance of the loop. This separation reduces LC resonance effects in the HFEMI band.

### C. SNR at High Frequency Relative to Coil Windings

Low-frequency EMI instruments use multiple turns in either the receiver or the transmitter to boost the received signal in proportion to the number of turns. However, at high frequency, the extra wire needed for multiple turns would corrupt the data, due to the electrically long antenna, as outlined in the previous section. Further, any gain from additional windings would be offset by inductive effects in our frequency regime.

To understand this, note that the inductance of a circular solenoid is given by  $L = \frac{(\mu_0 n^2 \pi a^2)}{b} K$  where  $a$  is the radius of the coil,  $b$  is the solenoid height, and  $n$  is the number of coil turns [38].  $K$  is the inductance reduction factor, a constant for the dimension of the coil. For a fixed-pitch solenoid, that is  $l = \frac{n}{b}$ , the relationship can be written  $L = (\mu_0 n l \pi a^2) K$ , to illustrate inductance scales linearly with additional coil turns,  $L \propto n$ .

As a result, the external magnetic field produced by the same solenoid, for a given current through the solenoid, scales linearly with additional turns. Modeling the transmitter coil as a series RL coil, for frequencies above the cutoff, i.e.,  $f > \frac{R}{2\pi L}$ , the extra field produced per Ampere is exactly offset by the gain in additional windings. Therefore, in the inductively-dominated regime for the transmit coil, there is no benefit to additional windings. The downside to additional windings is the distortion of the spatial distribution of the

primary magnetic field, as was discussed throughout Section II.

## IV. DATA PROCESSING

To arrive at usable data, one must take three data acquisitions. The first isolates instrumental background corresponding to additive noise, and is taken with the instrument over the ground; a second provides calibration and accounts for multiplicative sources of noise, this is done by adding a piece of ferrite near one lobe of the figure-8 receiver coil; a third records the object response plus background, which can be then be processed and interpreted based on the previous two. These three acquisitions we call “background”, “ferrite”, and “data”, respectively, and simple coupling schematics are shown in Figure 7.

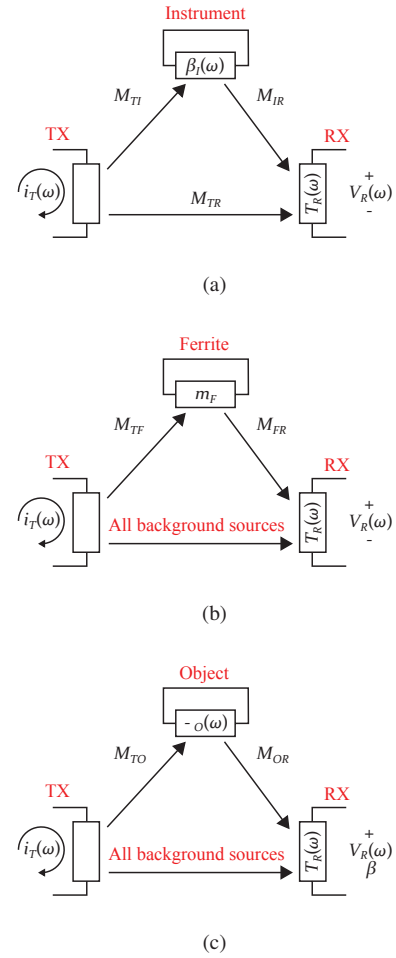


Fig. 7. (a) Background measurement. The direct coupling and instrument coupling are modeled as “All background sources” in the other two schematics. (b) Ferrite measurement. (c) Data measurement.

Using the ring model from Chilaka, et. al [33], we model the data for all three individual runs as

$$\hat{V}_R^{(B)} = \hat{i}_T^{(B)} (M_{TR} + M_{TI} \hat{\beta}_I M_{IR}) \hat{T}_R \quad (13)$$

$$\hat{V}_R^{(F)} = \hat{i}_T^{(F)} (M_{TR} + M_{TI} \hat{\beta}_I M_{IR} + M_{TF} m_F M_{FR}) \hat{T}_R \quad (14)$$

$$\hat{V}_R^{(O)} = \hat{i}_T^{(O)} (M_{TR} + M_{TI} \hat{\beta}_I M_{IR} + M_{TO} \hat{\beta}_O M_{OR}) \hat{T}_R \quad (15)$$



The measured quantities of Figure 7 and Equations 13-15 are  $\hat{i}_T$  and  $\hat{V}_R$ . These are, respectively, the transmit current and received voltage in the frequency domain. The superscripts of Equations 13, 14, and 15 (background - (B), ferrite - (F), and data - (O)) correspond to the measurements in Figures 7a, 7b, and 7c, respectively. Magnetic coupling between two points is given by an inductive coupling coefficient,  $M_{xy}$ , from a current in  $x$  to emf in  $y$ .  $T_R(\omega)$  is the transfer function of the receiver, from flux to output voltage. We use the symbol  $T$  instead of the traditional  $H$  to distinguish from magnetic field. The transfer function of the transmitter does not need to be considered in our analysis, because we can directly measure the current in the transmitter loop. For the reader's convenience, we put hats on quantities varying with frequency, i.e.,  $\hat{T} = T(\omega)$ . In other conditions, e.g., those involving seawater and larger observation distances, the coupling coefficients would also become frequency dependent, via non-negligible  $k$  values in equations such as 7, 8, and 9, as described in Section II-B.

#### A. Receiver Coil Transfer Function Compensation

The object's magnetic polarizability,  $\hat{\beta}_O$  (figure 7c), is buried within factors that affect the measured data. There are two different sources of obscuring unknowns for this type of measurement. Additive sources – residual primary field, ground response, and instrument self-response – combine in superposition with the measured data. The other unknown, a multiplicative one, arises from the transfer function of the receiver,  $\hat{T}_R$ . Therefore, with three unknowns (object, additive, and multiplicative), there are three measurements required to extract the object polarizability.

The additive and multiplicative factors are isolated by the background and ferrite measurements. The background is subtracted on a frequency-by-frequency basis, isolating additive factors. Next, to cancel the influence of the receiver coil transfer function, we divide by the ferrite response. The magnetic response of ferrite, which is magnetic and non-conductive, should be constant in our band, i.e.,  $m_F$  should not be a function of frequency. We can calculate a quantity proportional to the object response by

$$\hat{\beta}_O \propto \left( \frac{\hat{V}_R^{(O)}}{\hat{i}_T^{(O)}} - \frac{\hat{V}_R^{(B)}}{\hat{i}_T^{(B)}} \right) / \left( \frac{\hat{V}_R^{(F)}}{\hat{i}_T^{(F)}} - \frac{\hat{V}_R^{(B)}}{\hat{i}_T^{(B)}} \right) \quad (16)$$

where (B), (F), and (O) denote background, ferrite, and object, respectively.

Therefore, the quantity  $1/(\text{ferrite} - \text{background})$  is a mapping function to preserve the known “flatness” of the ferrite relaxation response, and is applied to data for anomalies.

### V. RESULTS

In this section we show experimental and numerical results for calibration targets and CF UXO. These data were taken using the one-turn, short-coiled prototype sensor, shown in Figure 6a. For each target the measured data are compared with analytic or numerical models.

Before illustrating these data, we should note some of the units given. In Figure 3b, the  $y$  axis has units of V·s/A, which is the measured voltage (V) divided by measured current (A)

in the Tx coil. Because the voltage is related to  $j\omega\vec{B}$ , and not the desired secondary  $\vec{B}$  field, we divide by  $j\omega$  (s) to extract magnetic field. These units were given because these data were prepared without calibrating by ferrite. Unlike those data, the figures shown in this section have  $y$  axes with units “Normalized Response”, which is the ratio of the measured signal to the secondary field produced by the magnetic and non-conducting ferrite. These values are arbitrary, for two reasons. Firstly, the mutual inductance constants described in Section II-B are parameters that vary with position, but not frequency. As such, they are unknown constants which add ambiguity to the overall measured amplitude. Secondly, ambiguity is added by scaling from the amplitude of the ferrite division. Thus, in this section, readers should only pay attention to the SNR and shape of the data, not their amplitudes in absolute terms.

#### A. Shotput

One common target for testing EMI instruments is a spherical conducting target. We placed a 4-in diameter steel sphere shotput approximately 1 inch under one lobe of the figure-8 coil. The measured high frequency and modeled EMI responses for the shotput are shown in Figure 8. The

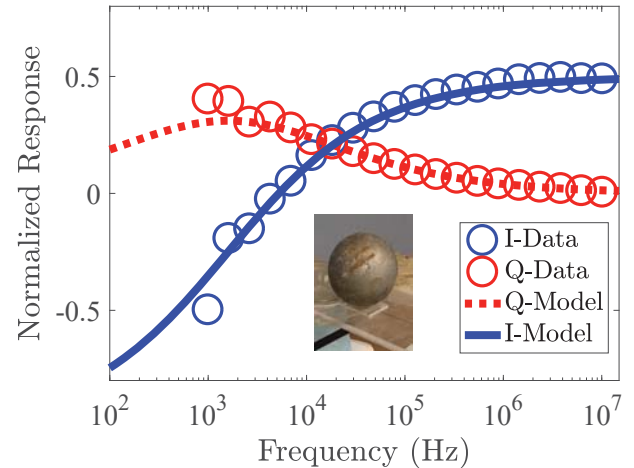


Fig. 8. HFEMI measurement taken over 4-in spherical steel shotput (conducting, permeable) contrasted with analytical magneto-quasistatic scattering solution. A photo of the target is overlaid on the graph.

measured quadrature EMI peak for the shotput, shown in Figure 8 is below the range we can reliably observe with the instrument. Namely, the low-frequency portion of the spectrum shows characteristic low SNR, despite using 5,000 waveforms stacked per frequency. This decreased SNR relative to traditional EMI sensors is attributable to the one-turn Tx and Rx coils as discussed in Section III-C. We modeled the broadband EMI response from the sphere using an analytical expression [3]. Using this analytical expression as a forward model, we estimated the conductivity and permeability to be  $4 \times 10^6$  S/m and 130, respectively. The model suggests reasonable agreement with the data at all frequencies.

### B. Carbon Fiber Plate

Another target we have used to test this HFEMI sensor is a sample plate of woven carbon fiber/epoxy composite. This plate is 4 mm thick, and 24 cm  $\times$  13.65 cm on the sides. For the data in Figure 9, this plate was measured 8 cm below one lobe of the figure-8 receiver. We stacked 5,000 waveforms for each frequency to achieve better SNR.

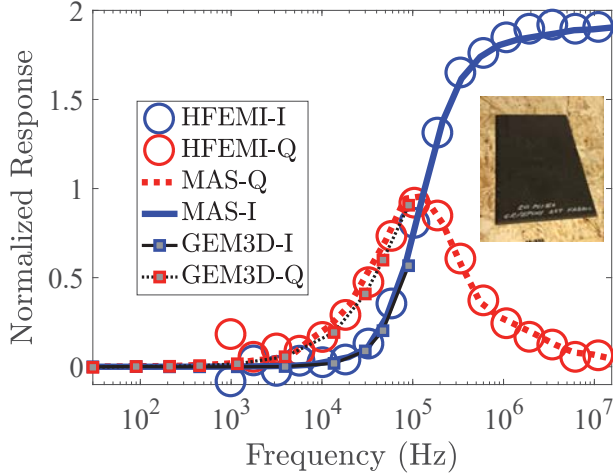


Fig. 9. Measured data, MAS numerical simulation, and GEM3D taken over 4 mm  $\times$  24 cm  $\times$  13.65 cm carbon-fiber plate (intermediate conducting, non-permeable,  $\sigma \approx 11,700$  S/m)

In order to compare our instrument's data to models, and vice versa, Figure 9 contains MAS model results and data from a different frequency-domain EMI sensor. The sensor we compare is the GEM-3D [39], a frequency-domain sensor with two transmitters in a bucking configuration and one vector receiver. We plot the  $H_z$  vector component from data acquired over the same plate, and scaled to match. For this non-canonical target, the EMI response of the carbon fiber plate is modeled by the MAS, which is a full-wave 3D solver described in [15]. Through inversion, we estimate the plate's conductivity to be  $\sigma = 11,700$  S/m.

### C. 105-mm Carbon Fiber UXO

Finally, in this section we present data from the HFEMI instrument used over a 39-cm long (without the nose), 105-mm CF UXO, and compare it with results from the MAS model, calculated using a body-of-revolution technique. The data in Figure 10 were collected during the first formal test of the HFEMI sensor at the Cold Regions Research and Engineering Laboratory (CRREL) in Hanover, NH, and are one part of a 3x3 grid test. The UXO was laid flat with its top surface 7.5 cm beneath the sensor and axis directed perpendicular to a line drawn through the centers of the two circles in the figure-8 receiver. One of the lobes of the figure-8 Rx coil was situated directly above the center of the UXO.

During the grid test, we decreased stacking for faster data acquisition. The data here contained 2,000 stacked waveforms, which are fewer than the number used for the plate and shotput, shown previously. Consequently, this larger target has

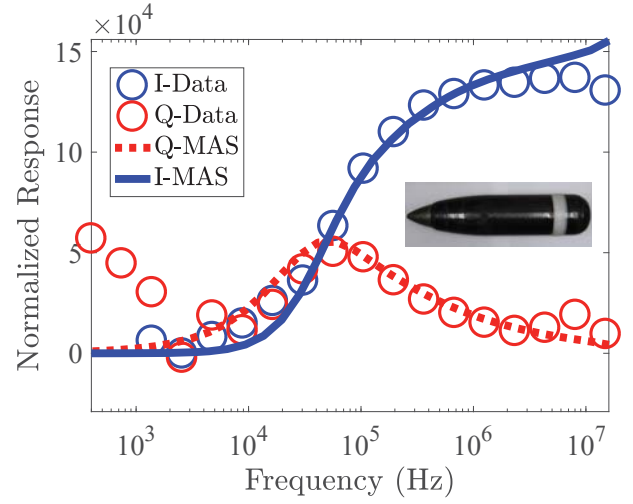


Fig. 10. Data collected over a CF 105 mm UXO (intermediate conducting, non-permeable,  $\sigma \approx 11,500$  S/m). This is the same target shown earlier in the paper, in Figure 3a.

worse SNR in the low frequencies. This UXO is a better representation of the type of targets that the HFEMI sensor will be used for in its eventual field use.

## VI. CONCLUSION

In this paper we have presented a new high frequency EMI instrument for sensing of IEC materials. The new HFEMI sensor extends the frequency band of traditional EMI sensors from 100 kHz to 15 MHz, and it can detect carbon fiber along with metallic targets.

We demonstrated that key to using this higher frequency range in an exclusively induction regime is guaranteeing that all aspects of the physical system stay electrically short throughout the operational frequency band. The transmitter and receiver coils must be constrained in length to maintain a single-phase current, meaning smaller, one-turn designs. In addition to the Tx field azimuthal inhomogeneity arising from Tx current nonuniformity due to the nonzero electrical length of the transmitter coil, using higher frequencies can expose effects which might not manifest for sensors operating in the traditional frequency range. These effects include RLC resonances, retarded time in coaxial cables, and changing amplifier gain and phase. These effects are mitigated through normalizing the acquired data by dividing by the frequency-domain response of a ferrite target.

We presented data recorded by the HFEMI prototype for three targets, and compared these to analytic and numerical models. These targets were a conducting and permeable steel sphere (shotput), an IEC material sample (CF plate), and an IEC UXO (105-mm CF UXO). As the US Military continues to develop and test CF munitions, proving grounds around the country will become contaminated with IEC UXO. These new targets, such as the smart bomb shown in our results, will require the HFEMI range for a complete description of their induction response.

The SNR of the single turn prototype instrument is decreased at the lower frequencies. To overcome this problem,



we are exploring methods to improve SNR at low frequency, but are still limited by the necessary shorter Tx and Rx coils. Future applications for the HFEMI instrument include sensing voids in conductive media such as soil.

#### ACKNOWLEDGMENT

This research was funded by the US Army Corps of Engineers, Engineer Research and Development Center, Environmental Quality and Installations Program, Contract W913E5-15-C-0006.

#### REFERENCES

- [1] "Carbon Fiber Bomb Saves Lives," <http://www.vallett.com/carbon-fiber-bomb-saves-lives/>.
- [2] S. A. Grant, B. E. Barrowes, F. Shubitidze, and S. A. Arcone, "Homemade explosives in the subsurface as intermediate electrical conductivity materials, a new physical principle for their detection," *Proc. SPIE*, vol. 9072, pp. 90 720A–90 720A–7, 2014. [Online]. Available: <http://dx.doi.org/10.1117/12.2050430>
- [3] J. R. Wait, "A conducting sphere in a time varying magnetic field," *Geophysics*, vol. 16, no. 4, pp. 666–672, 1951.
- [4] G. Olhoeft and D. Strangway, "Magnetic relaxation and the electromagnetic response parameter," *Geophysics*, vol. 39, no. 3, pp. 302–311, 1974.
- [5] D. K. Cheng, *Field and Wave Electromagnetics*. Addison-wesley New York, 1989, vol. 2.
- [6] F. S. Grant and G. F. West, *Interpretation Theory in Applied Geophysics*. McGraw-Hill Book, 1965.
- [7] J. Wait, *Geo-electromagnetism*. Elsevier, 2012.
- [8] F. Shubitidze, J. Fernandez, B. Barrowes, I. Shamatava, A. Bijamov, K. O'Neill, and D. Karkashadze, "The orthonormalized volume magnetic source model for discrimination of unexploded ordnance," *IEEE Transactions on Geoscience and Remote Sensing*, vol. 52, no. 8, pp. 4658–4670, Aug 2014.
- [9] J. McNeill, "Electromagnetic terrain conductivity measurement at low induction numbers," 1980.
- [10] C. O. Ao, H. Braunisch, K. O'Neill, and J. A. Kong, "Quasi-magnetostatic solution for a conducting and permeable spheroid with arbitrary excitation," *IEEE Transactions on Geoscience and Remote Sensing*, vol. 40, no. 4, pp. 887–897, Apr 2002.
- [11] B. Barrowes, K. O'Neill, T. Grzegorzczak, X. Chen, and J. Kong, "Broadband analytical magnetoquasistatic electromagnetic induction solution for a conducting and permeable spheroid," *IEEE Transactions on Geoscience and Remote Sensing*, vol. 42, no. 11, pp. 2479–2489, Nov 2004.
- [12] H. Braunisch, C. Ao, K. O'Neill, and J. Kong, "Magnetoquasistatic response of conducting and permeable prolate spheroid under axial excitation," *IEEE Transactions on Geoscience and Remote Sensing*, vol. 39, no. 12, pp. 2689–2701, Dec 2001.
- [13] K. O'Neill, *Discrimination of Subsurface Unexploded Ordnance*. SPIE Press, 2016.
- [14] F. Shubitidze, K. O'Neill, K. Sun, and I. Shamatava, "Application of broadband EMI responses to infer buried object's aspect ratio," in *Geoscience and Remote Sensing Symposium, 2002. IGARSS '02. 2002 IEEE International*, vol. 3, June 2002, pp. 1542–1545 vol.3.
- [15] F. Shubitidze, K. O'Neill, S. Haider, K. Sun, and K. Paulsen, "Application of the method of auxiliary sources to the wide-band electromagnetic induction problem," *IEEE Transactions on Geoscience and Remote Sensing*, vol. 40, no. 4, pp. 928–942, Apr 2002.
- [16] C. Ratto, P. Torriane, and L. Collins, "Exploiting ground-penetrating radar phenomenology in a context-dependent framework for landmine detection and discrimination," *IEEE Transactions on Geoscience and Remote Sensing*, vol. 49, no. 5, pp. 1689–1700, May 2011.
- [17] C.-C. Chen, M. Higgins, K. O'Neill, and R. Detsch, "Ultrawide-bandwidth fully-polarimetric ground penetrating radar classification of subsurface unexploded ordnance," *IEEE Transactions on Geoscience and Remote Sensing*, vol. 39, no. 6, pp. 1221–1230, June 2001.
- [18] G. R. Harbaugh, D. A. Steinhurst, J. B. Kingdon, T. Furuya, D. A. Keiswetter, T. H. Bell, and D. C. George, "EMI array for cued UXO discrimination," DTIC Document, Tech. Rep., 2010.
- [19] J. Fernandez, B. Barrowes, T. M. Grzegorzczak, N. Lhomme, K. O'Neill, and F. Shubitidze, "A man-portable vector sensor for identification of unexploded ordnance," *IEEE Sensors Journal*, vol. 11, no. 10, pp. 2542–2555, Oct 2011.
- [20] L.-P. Song, D. Oldenburg, L. Pasion, S. Billings, and L. Beran, "Temporal orthogonal projection inversion for EMI sensing of UXO," *IEEE Transactions on Geoscience and Remote Sensing*, vol. 53, no. 2, pp. 1061–1072, Feb 2015.
- [21] S. Billings, M. Cattach, and M. Laneville, "Detection of deep buried metal objects with the UltraTEM," *ASEG Extended Abstracts*, vol. 2015, no. 1, pp. 1–2, 2015.
- [22] C. Nelson, C. Cooperman, W. Schneider, D. Wenstrand, and D. Smith, "Wide bandwidth time-domain electromagnetic sensor for metal target classification," *IEEE Transactions on Geoscience and Remote Sensing*, vol. 39, no. 6, pp. 1129–1138, Jun 2001.
- [23] I. J. Won, D. Keiswetter, and T. Bell, "Electromagnetic induction spectroscopy for clearing landmines," *IEEE Transactions on Geoscience and Remote Sensing*, vol. 39, no. 4, pp. 703–709, Apr 2001.
- [24] J. P. Fernández, B. Barrowes, K. O'Neill, I. Shamatava, and F. Shubitidze, "A vector handheld frequency-domain sensor for UXO identification," *Proc. SPIE*, vol. 7303, pp. 73 030W–73 030W–12, 2009. [Online]. Available: <http://dx.doi.org/10.1117/12.818812>
- [25] D. L. Wright and W. C. Chew, "Enhancements to and characterization of the very early time electromagnetic (VETEM) prototype instrument and applications to shallow subsurface imaging at sites in the DOE complex," Environmental Management Science Program Workshop, Tech. Rep., 1998.
- [26] D. G. Smith and H. M. Jol, "Ground penetrating radar: antenna frequencies and maximum probable depths of penetration in Quaternary sediments," *Journal of Applied Geophysics*, vol. 33, no. 1, pp. 93–100, 1995.
- [27] B. K. Sternberg, "A new method of subsurface imaging-the LASI high frequency ellipticity system: Part 1. System design and development," *Journal of Environmental and Engineering Geophysics*, vol. 4, no. 4, pp. 197–213, 1999.
- [28] J. P. Fernández, B. E. Barrowes, T. M. Grzegorzczak, N. Lhomme, K. O'Neill, and F. Shubitidze, "A man-portable vector sensor for identification of unexploded ordnance," *IEEE Sensors Journal*, vol. 11, no. 10, pp. 2542–2555, 2011.
- [29] F. Shubitidze, J. Sigman, K. O'Neill, I. Shamatava, and B. Barrowes, "High frequency electromagnetic induction sensing for non-metallic ordnances detection," in *2014 XIXth International Seminar/Workshop on Direct and Inverse Problems of Electromagnetic and Acoustic Wave Theory (DIPED)*, Sept 2014, pp. 180–182.
- [30] F. Bogdanov, D. Karkashadze, and R. Zaridze, "The method of auxiliary sources in electromagnetic scattering problems," *Generalized Multipole Techniques for Electromagnetic and Light Scattering*, pp. 143–172, 1999.
- [31] "EMCoS," <https://www.emcos.com/>. [Online]. Available: <https://www.emcos.com/>
- [32] S. V. Chilaka, D. L. Faircloth, L. S. Riggs, and H. H. Nelson, "Enhanced discrimination among uxo-like targets using extremely low-frequency magnetic fields," *IEEE Transactions on Geoscience and Remote Sensing*, vol. 44, no. 1, pp. 10–21, Jan 2006.
- [33] V. S. Chilaka, "Electromagnetic induction systems for discrimination among metallic targets," Ph.D. dissertation, Auburn University, Auburn, Alabama, May 2006.
- [34] J. A. Stratton, *Electromagnetic Theory*. John Wiley & Sons, 2007.
- [35] J. Lindsay, "A circular loop antenna with nonuniform current distribution," *IRE Transactions on Antennas and Propagation*, vol. 8, no. 4, pp. 439–441, July 1960.
- [36] L.-W. Li, M.-S. Yeo, M.-S. Leong, and J. Kong, "Method of moments analysis of active thin circular loop antennas with closed-form currents and validity," *Journal of Electromagnetic Waves and Applications*, vol. 15, no. 11, pp. 1551–1569, 2001. [Online]. Available: <http://dx.doi.org/10.1163/156939301X00102>
- [37] T. H. Bell, B. J. Barrow, and J. T. Miller, "Subsurface discrimination using electromagnetic induction sensors," *IEEE Transactions on Geoscience and Remote Sensing*, vol. 39, no. 6, pp. 1286–1293, Jun 2001.
- [38] H. Wheeler, "Inductance formulas for circular and square coils," *Proceedings of the IEEE*, vol. 70, no. 12, pp. 1449–1450, Dec 1982.
- [39] K. O'Neill, "Project UX-1353: GEM-3D (SEED)," DTIC Document, Tech. Rep., 2004.